Excitation of high-frequency electromagnetic waves by energetic electrons with a loss cone distribution in a field-aligned potential drop

Shing F. Fung

Space Physics Data Facility, NASA Goddard Space Flight Center, Greenbelt, Maryland

Adolfo F. Viñas

Laboratory for Extraterrestrial Physics, NASA Goddard Space Flight Center, Greenbelt, Maryland

Abstract. The electron cyclotron maser instability (CMI) driven by momentum space anisotropy, $\partial f/\partial p_\perp > 0$, has been invoked to explain many aspects, such as the modes of propagation, harmonic emissions, and the source characteristics of the auroral kilometric radiation (AKR). Recent satellite observations of AKR sources indicate that the source regions are often imbedded within the auroral acceleration region characterized by the presence of a field-aligned potential drop. In this paper we investigate the excitation of the fundamental extraordinary mode radiation due to the accelerated electrons. The momentum space distribution of these energetic electrons is modeled by a realistic upward loss cone as modified by the presence of a parallel potential drop below the observation point. On the basis of linear growth rate calculations we present the emission characteristics, such as the frequency spectrum and the emission angular distribution as functions of the plasma parameters. We will discuss the implication of our results on the generation of the AKR from the edges of the auroral density cavities.

Introduction

The generation of high-frequency electromagnetic waves in the ordinary (O) and extraordinary (X) modes by an electron momentum space anisotropy, $\partial f/\partial p_\perp > 0$, has commonly been invoked to explain the observations of many natural radio emissions occurring in planetary magnetospheres and the solar corona [*Sharma et al.*, 1982; *Wu*, 1985, and references therein]. The best known example is perhaps the model for the generation of Earth's auroral kilometric radiation (AKR) from which the theory of the electron cyclotron maser instability (CMI) has been developed [*Wu and Lee*, 1979; *Wu*, 1985].

Wu and Lee [1979] pointed out that when the primary energetic (auroral) electrons precipitate into the ionosphere along the converging background magnetic field, the electrons with small pitch angles η will collide with ionospheric particles to excite auroral emissions and be lost from the primary electron population. Those energetic electrons with sufficiently large initial pitch angles will mirror back toward the magnetosphere, forming an upward loss cone distribution. It was thought that the loss cone distribution, exhibiting a momentum space anisotropy $\partial f/\partial p_\perp > 0$, would provide the free energy source for the CMI.

Considerable amount of theoretical work have contributed to the development of the CMI [see *Wu*, 1985, and references therein. *Le Quéau and Louarn*, 1989; *Wong et al.*, 1989; *Yoon and Krauss-Varban*, 1990; *Gaelzer et al.*, 1992; *Mourenas et al.*, 1993]. Most of these model calculations are based on the

Dory-Guest-Harris (DGH) distribution, $f_{DGH} \propto (p_\perp^2/\alpha^2)^l \exp[-(p/\alpha)^2]$ [*Dory et al.*, 1965], which does provide the necessary $\partial f/\partial p_\perp > 0$ to drive the instability, as does a true loss cone distribution. However, the DGH model distribution has a pathological artifact that for $-\infty \le p_\parallel \le \infty$, f_{DGH} tends to 0 as $p_\perp$ diminishes (Figure 1); and it tends to prescribe an exaggerated loss cone (compared to the observations shown in Figure 2a) and may thus lead to an overestimate of the CMI growth rate. Although the DGH distribution can model the steepness of the loss cone boundary, it is not amenable to studying the effects of parallel electric fields on the CMI.

Omidi and Gurnett [1982, 1984] calculated numerically the CMI growth rates based on typical electron loss cone distributions observed by the S3-3 satellite [*Croley et al.*, 1978]. They concluded that the observed loss cones are unstable. However, they found that the temporal growth rates γ associated with the observed loss cones are at least a factor of 10 smaller than a $\gamma/\Omega_{ce} \sim 10^{-3}$ typically needed to account for the observed AKR intensities, unless the unstable loss cones have relatively sharp loss cone boundaries (width $\sim 0.5°$), that is, large and positive $\partial f/\partial p_\perp$.

Recent AKR observations made by the Swedish Viking satellite indicate that there may be more than one free energy sources for the emission of AKR. In addition to the usual loss cone distribution [*Ungstrup et al.*, 1990], *Louarn et al.* [1990] argued that the trapped population of the auroral electrons are more likely to be the source of AKR. Moreover, *Hilgers et al.* [1992] analyzed the thermal electron measurements obtained within and near AKR source regions by the Viking satellite. They demonstrated that AKR source regions are depleted of thermal plasma and are likely located within the auroral acceleration regions.
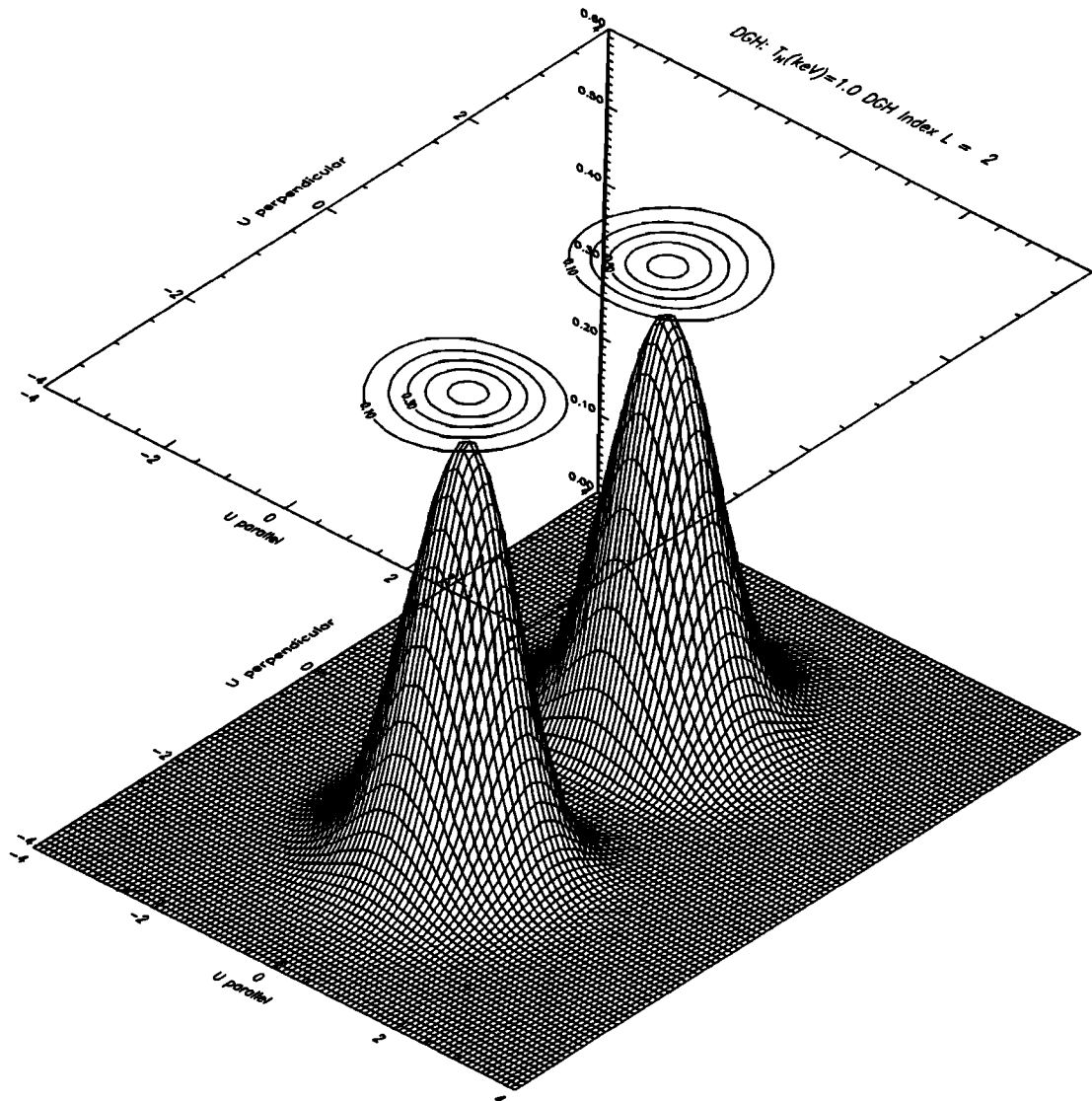
(a)

Figure 1. The Dory-Guest-Harris model distribution commonly used as an effective loss cone distribution for studying the electron cyclotron maser instability.

Persson [1966] showed that a quasi-neutral plasma equilibrium can be established by a quasistatic potential drop along a converging magnetic field. If such conditions exist inside the auroral acceleration regions, the field-aligned potential drops can modify the loss cone boundaries and lead to widening of the loss cones [*Croley et al.*, 1978; *Reiff et al.*, 1988]. *Wong et al.* [1982] and *Wu et al.*, [1982] pointed out that enhanced wave growths can result from both the depletion of the background plasma as well as the modified distribution caused by the presence of a parallel electric field. They demonstrated that the CMI growth rates can increase by about a factor of 3 as a result of a relatively large field-aligned potential drop (~7.5 keV) present below the source location. Their calculations indicate that growth rates of the order of $\gamma/\Omega_{ce} \sim 10^{-3}$ can be obtained when the energetic electrons dominate the plasma electron content and their dielectric effects are taken into consideration. Thus these results are compatible with the observations that AKR sources are located well within the auroral density cavity regions. However, the apparent successes of the existing

CMI models with a dominant energetic electron population tend to overshadow the possibility of radio emissions being generated near the edges of the density cavities or wherever the cold background plasma may remain to be the primary plasma electron component.

Persoon et al. [1988] analyzed the data from the plasma wave instrument (PWI) on the Dynamics Explorer (DE) 1 satellite and showed that the AKR and Z mode radiation are highly correlated with the density cavity structures in the auroral zone. AKR was found to occur inside as well as poleward of a density cavity in 97% of the 74 cavity intervals surveyed, while the Z mode radiation has a 78% occurrence rate. Furthermore, detailed analyses of three auroral events by *Persoon et al.* [1988] indicate that the energetic precipitating electrons (>1 keV) are insignificant compared to all the electron precipitation observed in the polar cap and poleward of the density cavities. On average, they constitute less than 25% of all the auroral electrons with only a slightly higher percentage concentration inside the cavity regions. The recent Viking observations reported by *Hilgers et al.*
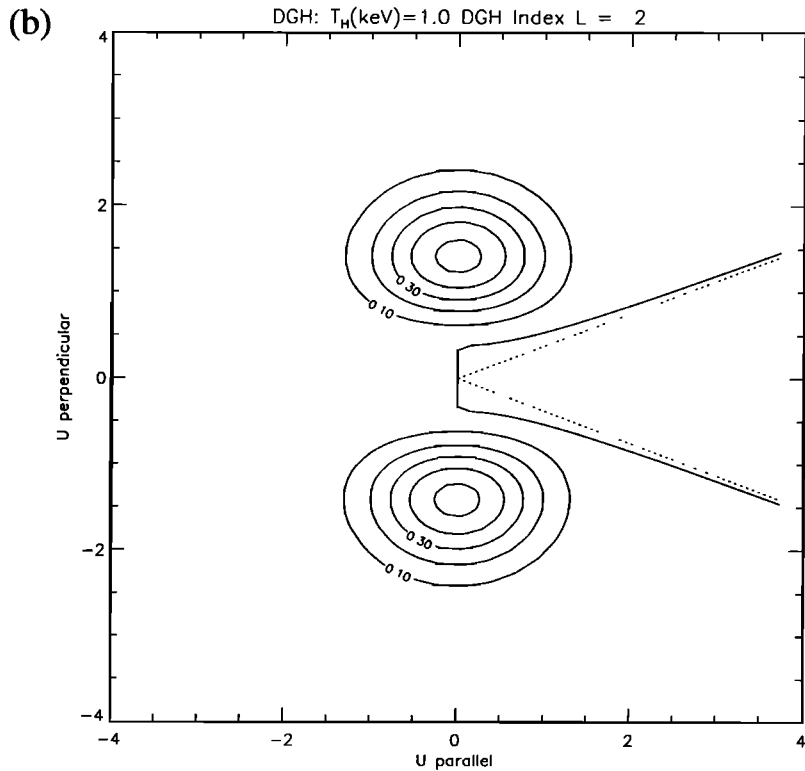
(b)

DGH: $T_H(keV)=1.0$ DGH Index $L = 2$

Figure 1. (continued)

[1992] also suggest that the energetic precipitating electrons may account for no more than a few percent of the auroral electrons near the edges of auroral density cavities.

We investigate in this paper the radio emissions excited by a tenuous population of energetic electrons with a realistic loss cone distribution. Our main objective is to study heuristically the effects of a quasi-static electric potential drop that may be present in the source region. Our results presented below show that the radio emissions generated from the edges of auroral density cavities can have intensities comparable to those excited near the centers of the cavities. Although both the ordinary (O) and extraordinary (X) mode waves can be excited, we concentrate in this paper only on the fundamental X mode waves, which is known to be the dominant mode to be excited by the CMI.

Model Distribution Function

As mentioned before, the DGH model distribution function, devised for stability studies of trapped particles in magnetic mirror fields, has often been adopted by investigations of the electron cyclotron instability. Its popularity arises for the most part from its characteristic momentum space anisotropy with $\partial f/\partial p_\perp > 0$ and its ease of analytical and numerical implementations. However, as pointed out by *Wu et al.* [1982], the DGH distribution is unrealistic for modeling the electron loss cone distribution as observed in the auroral zones [*Croley et al.*, 1978; *Menietti et al.*, 1993]. Other existing models of the loss cone are also unrealistic in one way or another [*Sharma et al.*, 1982; *Hewitt et al.*, 1982; *Wong et al.*, 1982; *Wu et al.*, 1982]. In these models the distribution functions are either completely evacuated in the loss cone and become discontinuous at the loss cone bound-

aries, contrary to observations, or they fail to correctly represent the changes of the loss cone boundaries by a parallel potential drop.

In the present study we have assumed for simplicity a plasma model in which all ion species are immobile and the plasma electrons consist of only a cold isotropic background component ($v_{th} \ll c$) and an energetic population having a drift loss cone distribution. We adopt a model distribution $F(u, \mu)$ that represents realistically the loss cone feature of the upward energetic electrons reflected by the ionosphere;

$$F(u, \mu) = A \exp\left[-\left(\frac{u - u_0}{\alpha}\right)^2\right] \qquad -1 \leq \mu \leq \mu_0 \qquad (1a)$$

$$F(u, \mu) = A \exp\left[-\left(\frac{u - u_0}{\alpha}\right)^2\right]$$

$$\cdot \exp\left[-\left(\frac{\mu - \mu_0}{\bar{\mu}}\right)^2\right] \qquad \mu_0 \leq \mu \leq 1 \qquad (1b)$$

where $u = p/m_0 = \gamma_L v$ is the relativistic electron momentum per unit rest mass (m_0) with $\gamma_L = [1 + (u/c)^2]^{1/2}$ being the Lorentz factor, u_0 is the characteristic momentum drift of the energetic electrons resulting from an acceleration above the observation point [*Gurgiolo and Burch*, 1988], α is the thermal spread of the energetic electron momenta and is related to the thermal energy T as $(\alpha/c)^2 = [(T/m_0 c^2) + 1]^2 - 1$, μ and μ_0 are the cosines of the energetic electron pitch angle and the loss cone angle, respectively, $\bar{\mu}$ is the characteristic "width" of the loss cone boundary, and A is the normalization factor.

As seen in (1a) and (1b), the distribution function is continuous across the loss cone boundary μ_0 with a charac-
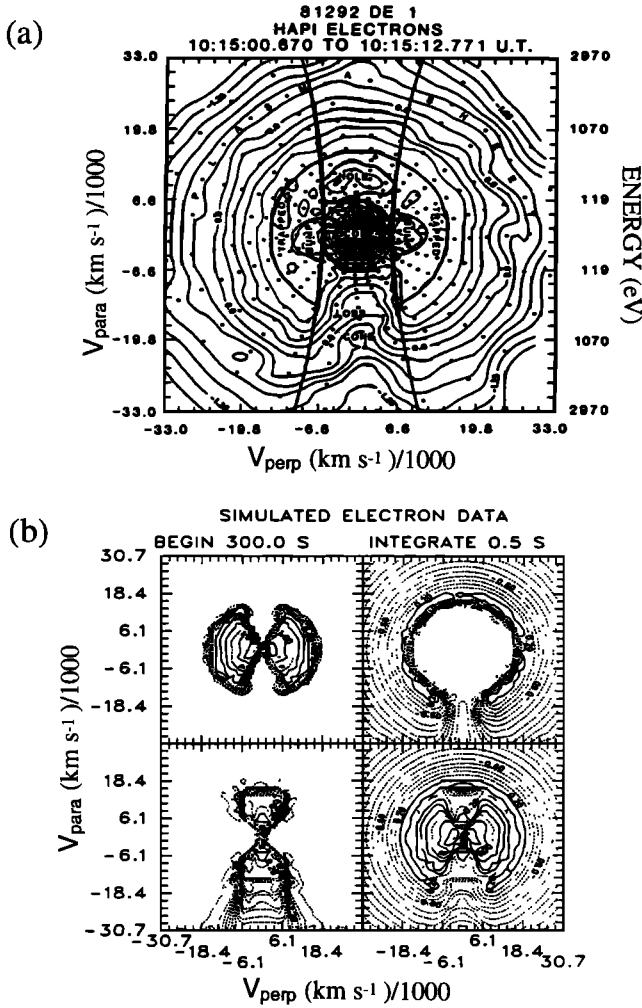
(a)

(b)

Figure 2. Electron velocity distribution (a) obtained by the DE 1 satellite at 14,000 km in the auroral zone (upper) and (b) simulated as resulting from two separated potential drops (lower) [from *Gurgiolo and Burch*, 1988].

invariants of the initially field-aligned energetic electrons [*Gurgiolo and Burch*, 1988; *Winglee and Pritchett*, 1986].

The width of the loss cone boundary $\bar{\mu}$ measures the steepness of the boundary wall and thus the emptiness of the loss cone interior. As shown by in situ particle observations [*Croley et al.*, 1978; *Gurgiolo and Burch*, 1988; *Menietti et al.*, 1993], the electron loss cones observed in the auroral zones are typically partially filled and have smooth boundaries. *Omidi and Gurnett* [1984] pointed out that the finite width of the loss cone boundary arises naturally from wave-particle interaction and collision processes along the auroral field lines and in the ionosphere. These scattering processes effectively introduce some "fuzziness" in the mirror points of the precipitating particles, thereby causing a spread in the loss cone boundary. Therefore $\bar{\mu}$ can be modeled by the uncertainty or the amount of "fuzziness" in the mirror point locations, $\Delta R_M/R_M$, of the reflected electrons after having suffered different amount of scattering. Then by differentiating (2) with respect to R_M, and substituting u^2 for simplicity by $\langle u^2 \rangle \approx \alpha^2$, the thermal spread of the energetic electrons, we obtain

$$\bar{\mu}(\alpha) = \frac{1}{2\mu_0(\alpha)} \left[1 + \frac{c^2}{\alpha^2} \left(\frac{e\Delta\Phi}{m_0 c^2} \right) \left(2\gamma_L(\alpha) + \frac{e\Delta\Phi}{m_0 c^2} \right) \right]$$

$$\cdot \left(\frac{R_M}{R} \right)^3 \left(\frac{\Delta R_M}{R_M} \right) \qquad (3)$$

Finally, with μ_0 and $\bar{\mu}$ given by (2) and (3), respectively, the distribution function (equations (1a) and (1b)) of the energetic electrons has a normalization factor A given by

$$A = \left\{ 2\pi \left[\int_0^\infty du (1 + \mu_0(u)) u^2 e^{-[(u-u_0/\alpha)]^2} \right. \right.$$

$$\left. \left. + \frac{\sqrt{\pi}}{2} \bar{\mu} \int_0^\infty du\, u^2 e^{-[(u-u_0/\alpha)]^2} \operatorname{erf} \left(\frac{1 - \mu_0(u)}{\bar{\mu}} \right) \right] \right\}^{-1} \qquad (4)$$

which must be computed numerically.

teristic width $\bar{\mu}$. When $u_0 = 0$ (Figures 3), the distribution function reduces to the model used by *Wu and Qiu* [1983]. If an upward parallel electric field is present in a converging magnetic field, such as a dipole field, the loss cone boundary at a radial distance R is widened according to the amount of potential drop $\Delta\Phi$ below the observing altitude [*Persson*, 1966; *Croley et al.*, 1978; *Reiff et al.*, 1988]. Then μ_0 in (1a) and (1b) is modified from its adiabatic value and becomes a function of u, $\Delta\Phi$, and the mirror ratio $B(R)/B_M = (R_M/R)^3$ (with subscript M denoting the mirror point):

$$\mu_0(u) = \left\{ 1 - \left(\frac{R_M}{R} \right)^3 \frac{c^2}{u^2} \left[\left(\gamma_L + \frac{e\Delta\Phi}{m_0 c^2} \right)^2 - 1 \right] \right\}^{1/2} \qquad (2)$$

Figure 4 shows the distribution function (equations (1a) and (1b)) with a finite u_0, representing the accelerated plasma sheet electrons. Note that the distribution function has the form of a partial shell outside the loss cone, similar to the simulation results (Figure 2b) obtained by *Gurgiolo and Burch* [1988] and the "banana" population observed by *Menietti et al.* [1993]. The shell-like feature may arise from pitch angle scattering and the conservation of adiabatic

Linear Growth Rate

We present in this section some calculations of the linear temporal growth rates γ of the CMI based on our model plasma and the distribution function given in (1)–(4). If the growth rates are small compared to the real angular frequencies ω_r of the unstable waves, that is, $\gamma \ll \omega_r$, then γ can be straightforwardly computed as [*Krall and Trievelpiece*, 1973]

$$\gamma = - \frac{D_i}{(\partial D_r/\partial \omega)} \bigg|_{\omega = \omega_r} \qquad (5)$$

where D_r and D_i are the real and imaginary parts of the dispersion function D, given by the determinant of the relativistic electromagnetic dispersion tensor

$$D_{ij} = n^2 \left(\frac{k_i k_j}{k^2} - \delta_{ij} \right) + \varepsilon_{ij} \qquad (6)$$

in which δ_{ij} is the Kronecher delta and $\varepsilon_{ij}(i, j = x, y, \text{ or } z)$ is the dielectric tensor [*Montgomery and Tidman*, 1964; *Tsai et al.*, 1981; *Stix*, 1992]
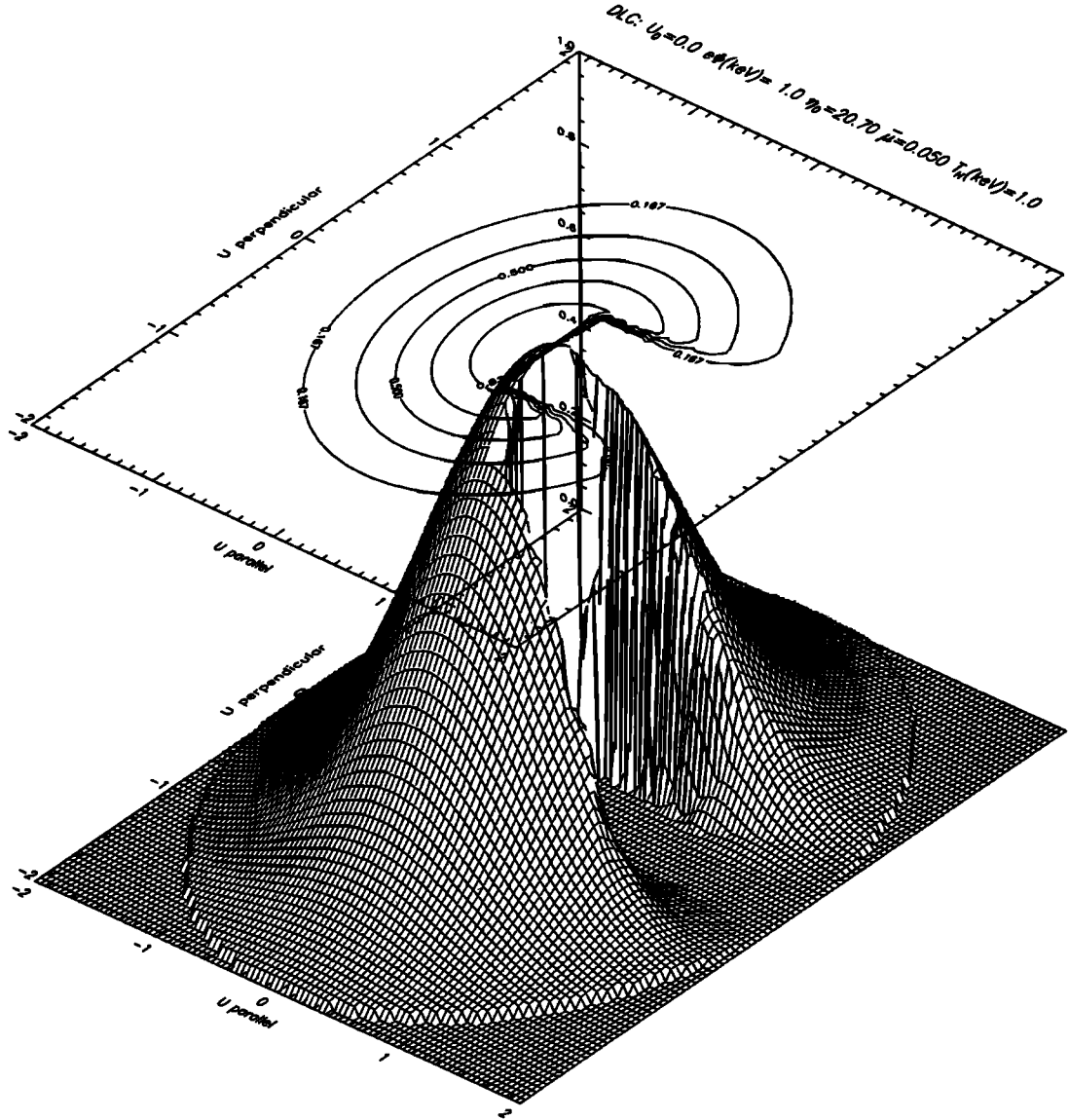
(a)

Figure 3. Drift-loss cone distribution with $u_0 = 0$ evacuated by a 1 kV potential drop below the observation altitude.

$$\varepsilon_{ij} = \delta_{ij} + \chi_{sij} = \delta_{ij} + 2\pi \sum_{s=\text{species}} \frac{\omega_{ps}^2}{\omega^2} \int_0^\infty du$$

$$\cdot \int_{-1}^1 d\mu \sum_{m=-\infty}^\infty \frac{\Lambda_{sij}^{(m)}}{\gamma_L \omega - m\Omega_s - k_\parallel u \mu} F_s(u, \mu) \qquad (7)$$

where χ_{sij} are the elements of the electric susceptibility tensor for the sth particle species, with

in which σ_s is the sign of the charge q_s, $\omega_{ps}^2 = (4\pi n_s q_s^2)/m_{0s}$ and $\Omega_s = |q_s|B/m_{0s}c$, are the angular plasma and gyrofrequency, respectively, $J_m = J_m(\lambda_s)$ are the mth order Bessel functions, $J'_m = dJ_m(\lambda_s)/d\lambda_s$ with $\lambda_s = k_\perp u(1 - \mu^2)^{1/2}/\Omega_s$, and

$$\Phi_1 = \omega u \frac{\partial}{\partial u} + \left(\frac{k_\parallel u}{\gamma_L} - \omega\mu \right) \frac{\partial}{\partial \mu}$$

$$\Lambda_s^{(m)} = \begin{bmatrix} \dfrac{n^2\Omega_s^2}{k_\perp^2} J_m^2 \Phi_1 & i\dfrac{m\sigma_s\Omega_s}{k_\perp} u\sqrt{1-\mu^2} J_m J'_m \Phi_1 & \dfrac{m\Omega_s}{k_\perp} u\mu J_m^2 \Phi_1 \\[3mm] -i\dfrac{m\sigma_s\Omega_s}{k_\perp} u\sqrt{1-\mu^2} J_m J'_m \Phi_1 & u^2(1-\mu^2) J_m'^2 \Phi_1 & -i\sigma_s u^2 \mu\sqrt{1-\mu^2} J_m J'_m \Phi_1 \\[3mm] \dfrac{m\Omega_s}{k_\perp} u\mu J_m^2 \Phi_1 & i\sigma_s u^2 \mu\sqrt{1-\mu^2} J_m J'_m \Phi_1 & u^2\mu^2 J_m^2 \Phi_2 \end{bmatrix} \qquad (8)$$
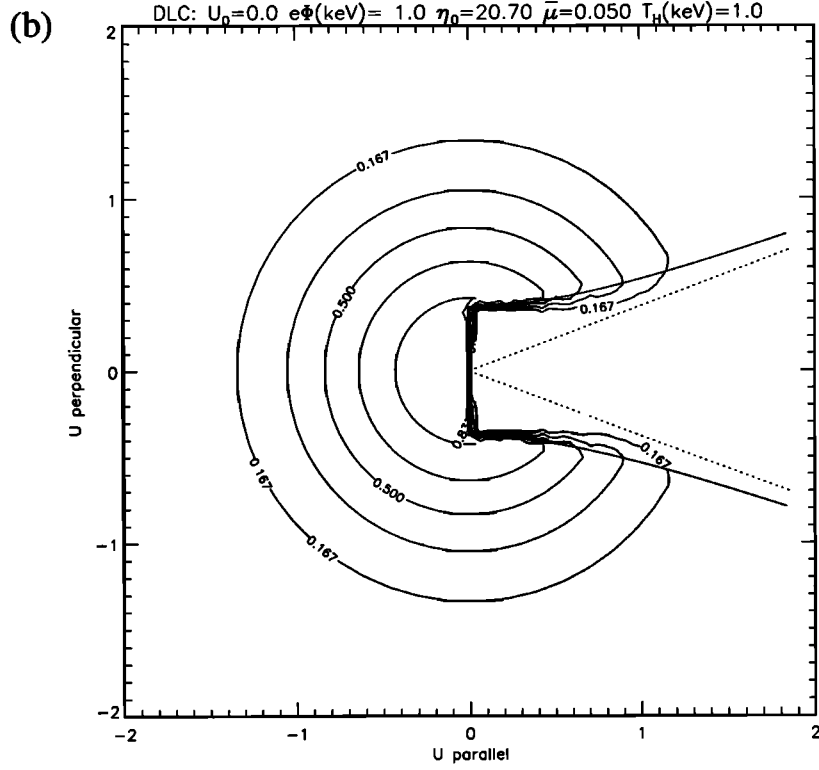
(b)

DLC: U_0=0.0   eΦ(keV)= 1.0 η_0=20.70 $\bar{\mu}$=0.050 T_H(keV)=1.0

Figure 3. (continued)

$$\Phi_2 = \Phi_1 + \left(\frac{\gamma_L \omega - m\Omega_s - k_\parallel \mu \mu}{\gamma_L \mu} \right) \frac{\partial}{\partial \mu}$$

As mentioned earlier, some applications of the plasma model presented here will accommodate the assumption that the energetic electron concentration (n_h) is small compared to that of the cold background electrons (n_c); that is, $n_h/n_c \ll 1$. In this case the dispersion function D for waves propagating in the x-z plane (with $k_x = k_\perp = k \sin \theta$ and $k_z = k_\parallel = k \cos \theta$) in a plasma with a background magnetic field $\mathbf{B} = B \, \hat{z}$ is given by [Stix, 1992]

$$+ (\varepsilon_1^2 - \varepsilon_2^2) \sin^2 \theta]n^2 + \varepsilon_3(\varepsilon_1^2 - \varepsilon_2^2) \tag{11}$$

which, in the high-frequency limit, $D_r = 0$ yields the familiar expression for the refractive index $n = kc/\omega$ as

$$n^2 = \left(\frac{kc}{\omega_r}\right)^2 = 1 - [2\omega_{pc}^2(\omega_r^2 - \omega_{pc}^2)/\omega_r^2]/\{2(\omega_r^2 - \omega_{pc}^2)$$

$$-\Omega_c^2 \sin^2 \theta \pm \Omega_c[\Omega_c^2 \sin^4 \theta + 4\omega_r^{-2}(\omega_r^2 - \omega_{pc}^2)^2 \cos^2 \theta]^{1/2}\}^{-1} \tag{12}$$

$$D = \det D_{ij} = \begin{vmatrix} -n^2 \cos^2 \theta + \varepsilon_1 + \delta\chi_{hxx} & i(\varepsilon_2 + \delta\chi_{hxy}) & n^2 \cos \theta \sin \theta + \delta\chi_{hxz} \\ -i(\varepsilon_2 + \delta\chi_{hxy}) & -n^2 + \varepsilon_1 + \delta\chi_{hyy} & \delta\chi_{hyz} \\ n^2 \cos \theta \sin \theta + \delta\chi_{hxz} & -\delta\chi_{hyz} & -n^2 \sin^2 \theta + \varepsilon_3 + \delta\chi_{hzz} \end{vmatrix} \tag{9}$$

where $\delta\chi_{hij}$ are the susceptibility elements due to the tenuous energetic electrons, and

$$\varepsilon_1 = 1 - \frac{\omega_{pc}^2}{\omega^2 - \Omega_c^2}, \quad \varepsilon_2 = \frac{\omega_{pc}^2 \Omega_c}{\omega(\omega^2 - \Omega_c^2)}, \quad \varepsilon_3 = 1 - \frac{\omega_{pc}^2}{\omega^2}. \tag{10}$$

such that the real dispersion function is determined by the dominant cold background plasma,

$$D_r = (\varepsilon_1 \sin^2 \theta + \varepsilon_3 \cos^2 \theta)n^4 - [\varepsilon_1\varepsilon_3(1 + \cos^2 \theta)$$

where the plus or minus sign in the denominator of (12) refers to the ordinary/extraordinary mode of propagation, respectively.

The imaginary part of $D(D_i)$ is given by the imaginary part of (9) in which $\delta\chi_{hij}$ are computed by substituting the drift-loss cone distribution of (1) into the second term of (7). These results and the derivative of D_r(11) with respect to ω can now be substituted into (5) to give an expression of the CMI linear temporal growth rate,
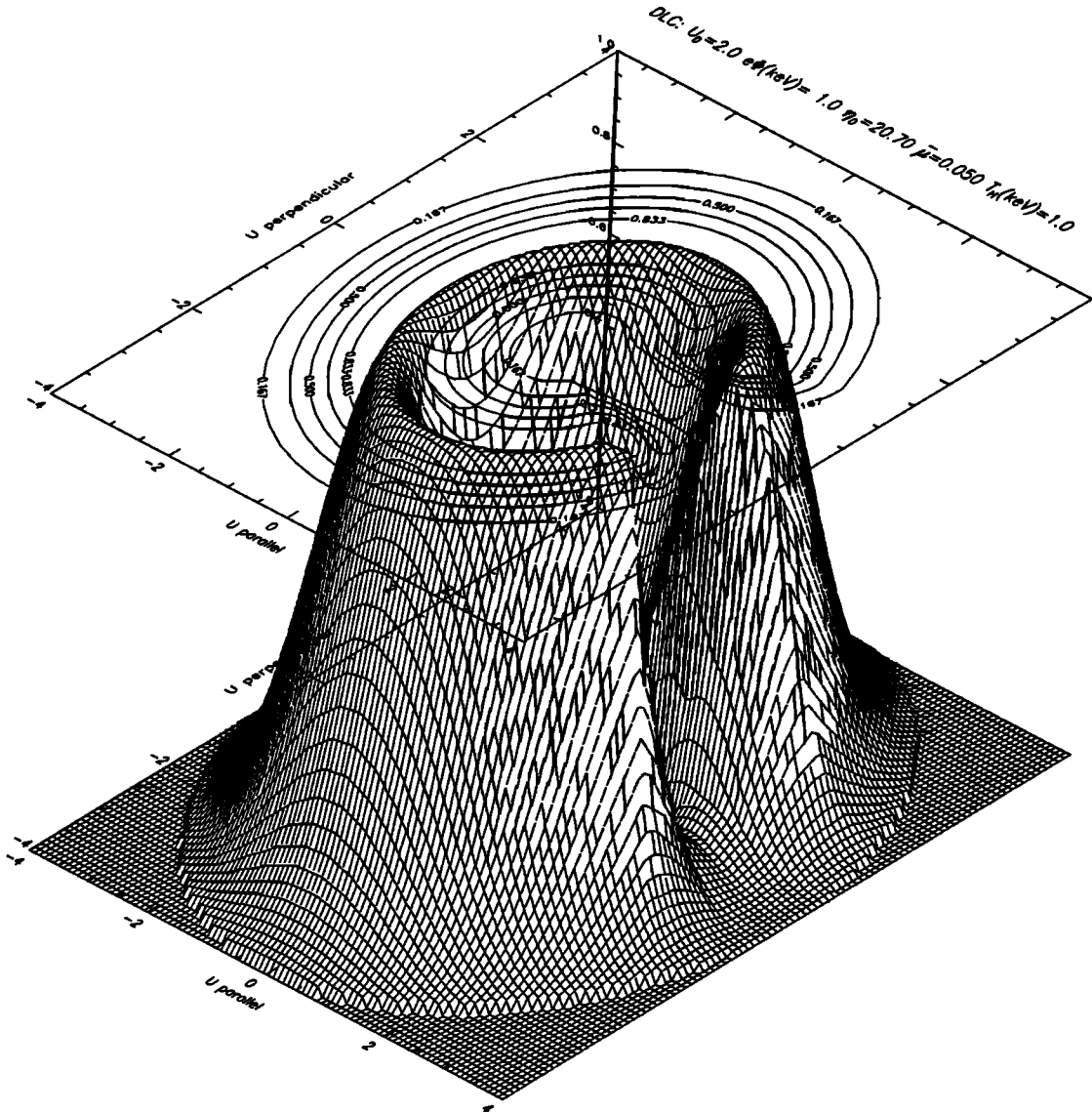
(a)

Figure 4. Drift-loss cone distribution with $u_0 = 2$, resembling the accelerated plasma sheet electrons (see Figures 2a and 2b).

$$\frac{\gamma}{\omega_r} = \left(\frac{n_h}{n_c}\right)$$

$$\cdot \frac{p_{xx}Q_{xx} + p_{yy}Q_{yy} + p_{zz}Q_{zz} + p_{xz}Q_{xz} + p_{xy}Q_{xy} + p_{yz}Q_{yz}}{G(\omega_r, \mathbf{k})} \quad (13)$$

where

$$p_{xx} = n^4 \sin^2 \theta - n^2(\varepsilon_3 + \varepsilon_1 \sin^2 \theta) + \varepsilon_1\varepsilon_3$$
$$p_{yy} = -n^2(\varepsilon_3 \cos^2 \theta + \varepsilon_1 \sin^2 \theta) + \varepsilon_1\varepsilon_3$$
$$p_{zz} = n^4 \cos^2 \theta - n^2\varepsilon_1(1 + \cos^2 \theta) + \varepsilon_1^2 - \varepsilon_2^2$$
$$p_{xy} = 2\varepsilon_2(\varepsilon_3 - n^2 \sin^2 \theta)$$
$$p_{xz} = 2n^2(n^2 - \varepsilon_1) \sin \theta \cos \theta$$
$$p_{yz} = 2n^2\varepsilon_2 \sin \theta \cos \theta$$

$$Q_{xx} = 2\pi^2 \frac{\omega_{pc}^2}{\omega_r^2} \int_0^\infty du$$

$$\cdot \sum_{m=-\infty}^{\infty} \frac{2m^2\Omega_c^2}{k_\perp^2} \{[K_1 J_m^2(\lambda_h)]_{-1 \le \mu_r \le \mu_0}$$

$$+ [K_2 J_m^2(\lambda_h)]_{\mu_0 \le \mu_r \le 1}\}$$

$$Q_{yy} = 2\pi^2 \frac{\omega_{pc}^2}{\omega_r^2} \int_0^\infty du$$

$$\cdot \sum_{m=-\infty}^{\infty} 2u^2\{[K_1(1 - \mu_r^2){J'_m}^2(\lambda_h)]_{-1 \le \mu_r \le \mu_0}$$

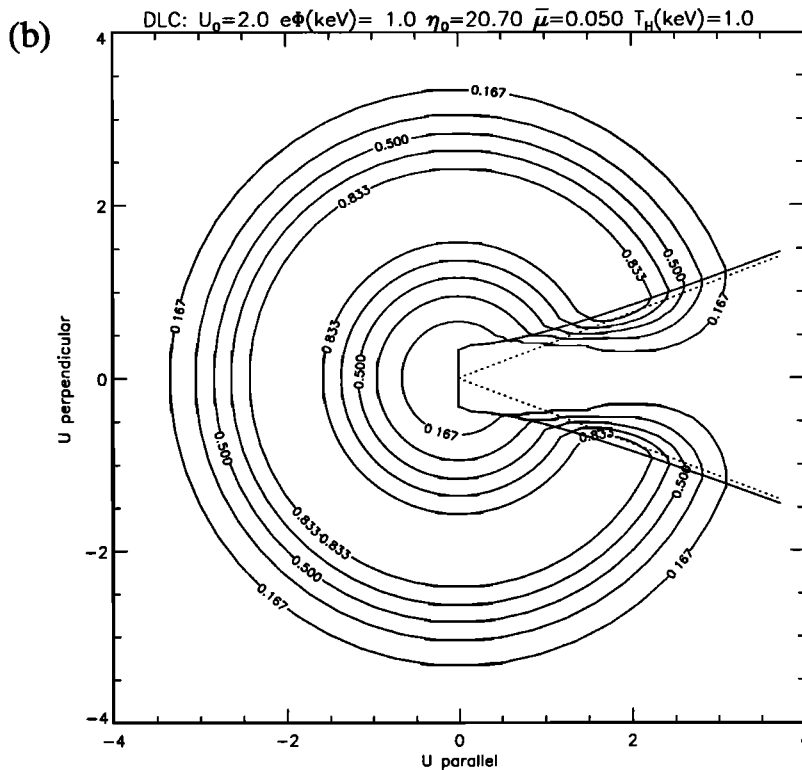$$+ [K_2(1 - \mu_r^2){J'_m}^2(\lambda_h)]_{\mu_0 \le \mu_r \le 1}\}$$

(b)

Figure 4. (continued)

$$Q_{zz} = 2\pi^2 \frac{\omega_{pc}^2}{\omega_r^2} \int_0^\infty du \sum_{m=-\infty}^{\infty} 2u^2\{[K_1\mu_r^2 J_m^2(\lambda_h)]_{-1\leq\mu_r\leq\mu_0}$$

$$+ [K_2\mu_r^2 J_m^2(\lambda_h)]_{\mu_0\leq\mu_r\leq1}\}$$

$$Q_{xy} = 2\pi^2 \frac{\omega_{pc}^2}{\omega_r^2} \int_0^\infty du \sum_{m=-\infty}^{\infty} \frac{2m\Omega_c u}{k_\perp}$$

$$\cdot \left\{ \begin{matrix} [K_1\sqrt{1 - \mu_r^2}J_m(\lambda_h)J_m'(\lambda_h)]_{-1\leq\mu_r\leq\mu_0} & + \\ [K_2\sqrt{1 - \mu_r^2}J_m(\lambda_h)J_m'(\lambda_h)]_{\mu_0\leq\mu_r\leq1} \end{matrix} \right\}$$

$$Q_{yz} = -2\pi^2 \frac{\omega_{pc}^2}{\omega_r^2} \int_0^\infty du \sum_{m=-\infty}^{\infty} 2u^2$$

$$\cdot \left\{ \begin{matrix} [K_1\mu_r\sqrt{1 - \mu_r^2}J_m(\lambda_h)J_m'(\lambda_h)]_{-1\leq\mu_r\leq\mu_0} & + \\ [K_2\mu_r\sqrt{1 - \mu_r^2}J_m(\lambda_h)J_m'(\lambda_h)]_{\mu_0\leq\mu_r\leq1} \end{matrix} \right\}$$

$$Q_{xz} = 2\pi^2 \frac{\omega_{pc}^2}{\omega_r^2} \int_0^\infty du \sum_0^\infty \frac{2m\Omega_c u}{k_\perp} \{[K_1\mu_r J_m^2(\lambda_h)]_{-1\leq\mu_r\leq\mu_0}$$

$$+ [K_2\mu_r J_m^2(\lambda_h)]_{\mu_0\leq\mu_r\leq1}\}$$

in which $\lambda_h = k_\perp u(1 - \mu_r^2)^{1/2}/\Omega_c$,

$$K_1 = A \frac{\omega_r(u - u_0)}{|k_\parallel|\alpha^2} \exp\left[-\left(\frac{u - u_0}{\alpha}\right)^2\right]$$

$$K_2 = A\left[\frac{\omega_r(u - u_0)}{|k_\parallel|\alpha^2} + \frac{(\mu_r - \mu_0)}{\bar{\mu}^2|k_\parallel u|}\left(\frac{k_\parallel u}{\gamma_L} - \omega_r\mu_r\right)\right]$$

$$\cdot \exp\left[-\left(\frac{u - u_0}{\alpha}\right)^2\right]\exp\left[-\left(\frac{\mu - \mu_0}{\bar{\mu}}\right)^2\right]$$

$$\mu_r = \frac{\gamma_L\omega_r - m\Omega_c}{k_\parallel u}$$

$$G = 2n^4\left[\frac{\omega_r^2\omega_{pc}^2 \sin^2 \theta}{(\omega_r^2 - \Omega_c^2)^2} + \frac{\omega_{pc}^2 \cos^2 \theta}{\omega_r^2}\right]$$

$$+ 4n^2\left[\frac{\omega_{pc}^2(\omega_{pc}^2 - \Omega_c^2)}{(\omega_r^2 - \Omega_c^2)^2} - 1 - \frac{\omega_{pc}^2\Omega_c^2 \sin^2 \theta}{2(\omega_r^2 - \Omega_c^2)^2}\right]$$

$$+ 2\left[\left(2 - \frac{\omega_{pc}^2}{\omega_r^2}\right)\left(1 - \frac{\omega_{pc}^2}{\omega_r^2 - \Omega_c^2}\right)^2 - \frac{\omega_{pc}^4\Omega_c^2}{\omega_r^2(\omega_r^2 - \Omega_c^2)^2}\right]$$

$$+ 2\left(1 - \frac{\omega_{pc}^2}{\omega_r^2}\right)^2 \frac{\omega_r^2\omega_{pc}^2}{(\omega_r^2 - \Omega_c^2)^2}\right]$$

n is given by (12); the normalization factor A, μ_0 and $\bar{\mu}$ are given by (2)–(4), respectively; and G is the same factor as given by *Wu and Qiu* [1983]. We note here also that a number of typographical errors contained by *Wu and Qiu* [1983] have been corrected in our derivation of (13). In addition, we have replaced Ω_h in Q_{ij} and μ_r by Ω_c.

Results and Discussions

We now investigate the conditions in which large CMI growth rates, such as that required ($\gamma/\Omega_{ce} \sim 10^{-3}$) for the generation of AKR [Omidi and Gurnett, 1982, 1984], can result from an unstable loss cone distribution given by (1a) and (1b). We have calculated the linear temporal growth rates of the CMI in the limit of small density ratios, $n_h/n_c \ll 1$, by numerically evaluating (13). For the frequencies of interest the $m = \pm 1$ terms in the infinite sums in (13) have the most significant contributions. Thus it is sufficient to numerically calculate the growth rates by keeping only the $m = 0$, ± 1, and ± 2 terms. The plasma model parameter sets used in the following growth rate calculations shown in Figures 5–9 are summarized in Table 1. To facilitate comparison of our results with observations in which only the wave frequencies are measured, we have chosen to present our calculated growth rates as a function of the wave frequency ω_r instead of the wave number k.

For the case of zero potential drop, $\Delta\Phi = 0$, Figures 5a and 5b display the normalized CMI growth rates of the fundamental extraordinary mode waves in various wave normal angles as a function of wave frequency ω_r/Ω_{ce} for $T_h = 2$ keV (Figure 5a) and $T_h = 10$ keV (Figure 5b), respectively. In this case the loss cone angle (equation (2)) is determined only by the magnetic mirror ratio (at $R = 1.5R_E$ in these examples).The resulting growth rate decreases as the wave normal angle increases. Figures 5a and 5b also indicate that high growth rates, reaching $\gamma/\Omega_{ce} \sim 10^{-3}$ for $n_h/n_c \approx 10^{-2}$, can be attained from high thermal energies of the energetic particles. In addition, the frequency bandwidth of the unstable waves propagating at a given wave normal angle also decreases as a result of higher temperature.

Figures 6 and 7 illustrate the effects of varying $\bar{\mu}$ and $\Delta\Phi$ (equation (3)) on the growth rates. The parameters used in Figure 6 are the same as in Figure 5b except that $\Delta R_M/R_M$ is increased from 0.025 for a relatively empty loss cone with sharp boundaries to 0.63 for a partially filled loss cone with smooth boundaries. Figure 6a shows the case of $e\Delta\Phi/m_0c^2 = 0.0$ as in Figure 5b. Even at relatively high T_h (10 keV), the larger $\bar{\mu}$ as a result of increased $\Delta R_M/R_M$ clearly leads to reduced growth rates due to the smaller $\partial f/\partial u_\perp$ associated with the larger $\bar{\mu}$.

Figure 6b shows for the same $\Delta R_M/R_M$ the effects of a moderate potential drop, $e\Delta\Phi/m_0c^2 = 0.01$ (corresponding to a 5 kV potential drop). As discussed by Omidi and Gurnett [1982, 1984], the widened loss cone due to the finite potential drop (equation (2)) encloses a larger portion of a given resonance ellipse, and should result in higher CMI growth rates. However, compared to the zero potential drop case (Figure 6a), only slight increases in growth rates were obtained. Although higher growth rates are possible when $n_h/n_c > 1$, Wong et al. [1982] and Wu et al. [1982] have in fact obtained less than a factor of 10 increase in the CMI growth rates when the assumed potential drop below the observation point exceeds 7 kV; whereas typical potential drops observed below the altitude of $2R_E$ in the auroral zone tend to vary only between 1 and 3 kV [Reiff et al., 1988]. Therefore much larger potential drops are required to yield a significant growth rate enhancement. In the case of Figure 6b it appears that the enhanced growth rates are also suppressed by the slightly larger $\bar{\mu}$ due to the finite potential drop (see (3) and Table 1).

Table 1. Parameters Used for Calculating the Growth Rates in Figures 5-9

	Figure									
	5a	5b	6a	6b	7a	7b	8a	8b	9a	9b
ω_{pe}/Ω_{ce}	0.2	0.2	0.2	0.2	0.2	0.2	0.2	0.2	0.15	0.15
R, R_E	1.5	1.5	1.5	1.5	1.5	1.5	**2.0**	2.0	2.0	2.0
$e\Delta\Phi/m_ec^2$	0.0	0.0	**0.0**	**0.01**	**0.002**	**0.01**	**0.0**	**0.01**	0.0	0.01
$\Delta R_M/R_M$	0.025	0.025	**0.63**	0.63	**0.063**	0.063	0.05	0.05	0.03	0.63
T_h, keV	2.0	**10.0**	10.0	10.0	5.0	5.0	1.0	1.0	1.0	0.5
u_0/α	0.0	0.0	0.0	0.0	0.0	0.0	4.0	4.0	3.0	6.0
$\bar{\mu}$	4.415×10^{-3}	4.415×10^{-3}	**0.1112**	0.1140	1.118×10^{-2}	1.140×10^{-2}	3.341×10^{-3}	3.413×10^{-3}	4.879×10^{-3}	4.300×10^{-2}
A	0.195	0.195	0.186	0.2023	0.2018	0.2312	2.807×10^{-3}	2.839×10^{-3}	2.004×10^{-3}	1.259×10^{-3}

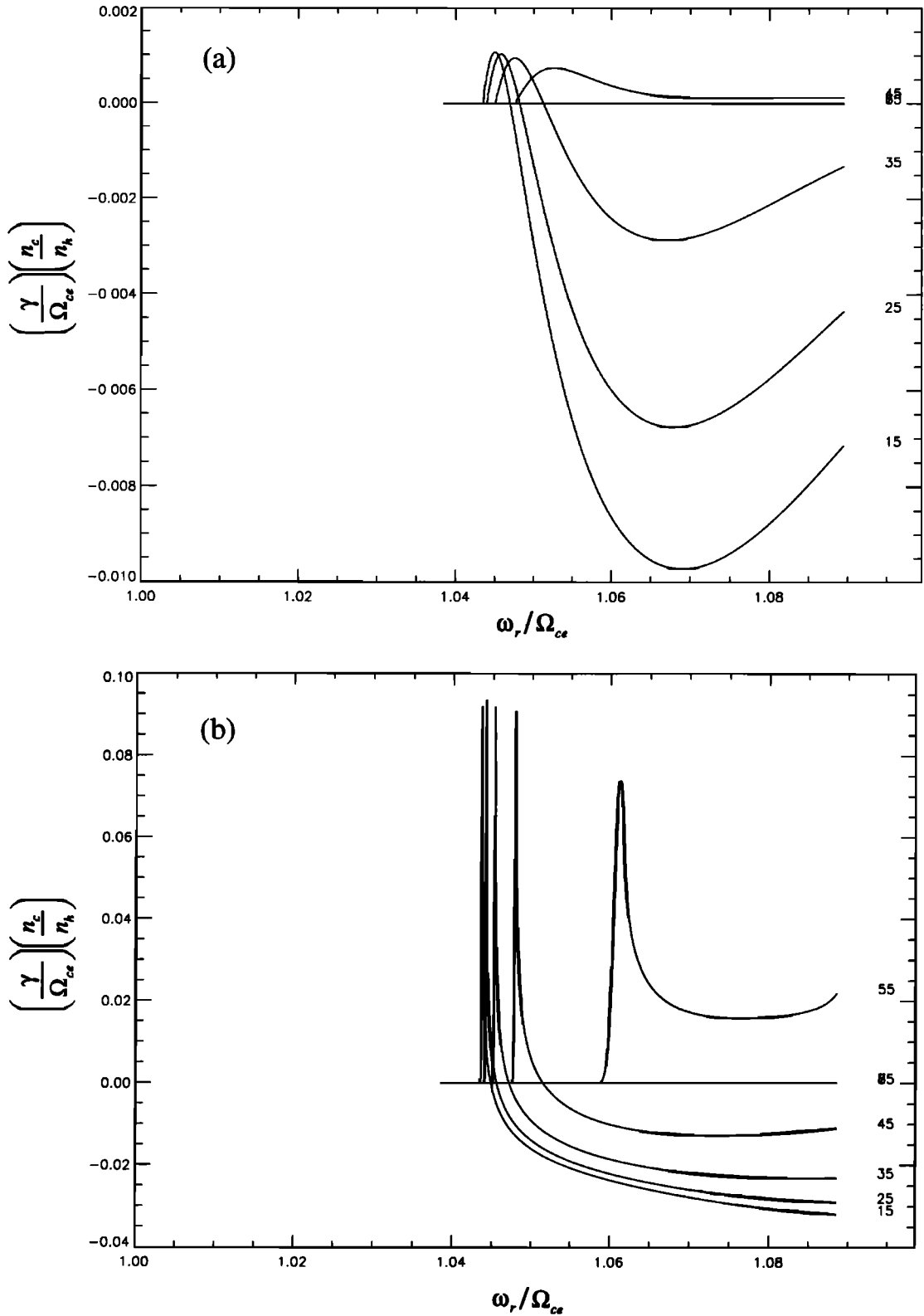Values in bold indicate the changes in the corresponding parameters.

Figure 5. Normalied CMI growth rates, $(\gamma/\Omega_{ce})(n_c/n_h)$, as a function of wave frequency ω_r/Ω_{ce} for various wave normal angles: 15°, 25°, 35°, 45°, 55°, 65°, and 75° with (a) $T_h = 2$ keV and (b) $T_h = 10$ keV.

If a sharp loss cone boundary ($\bar{\mu} \approx 10^{-2}$, $T_h = 5$ keV, $\Delta R_M/R_M = 0.063$; Table 1) is maintained, however, a field-aligned potential drop below the observation point tends to enhance only the damping by the energetic elec-

trons, see for example the growth rate curves at 45° wave normal angle in Figure 7a for $e\Delta\Phi/m_0c^2 = 0.002$ and Figure 7b for $e\Delta\Phi/m_0c^2 = 0.01$, respectively. This can be understood by realizing that a loss cone with a sharp boundary is
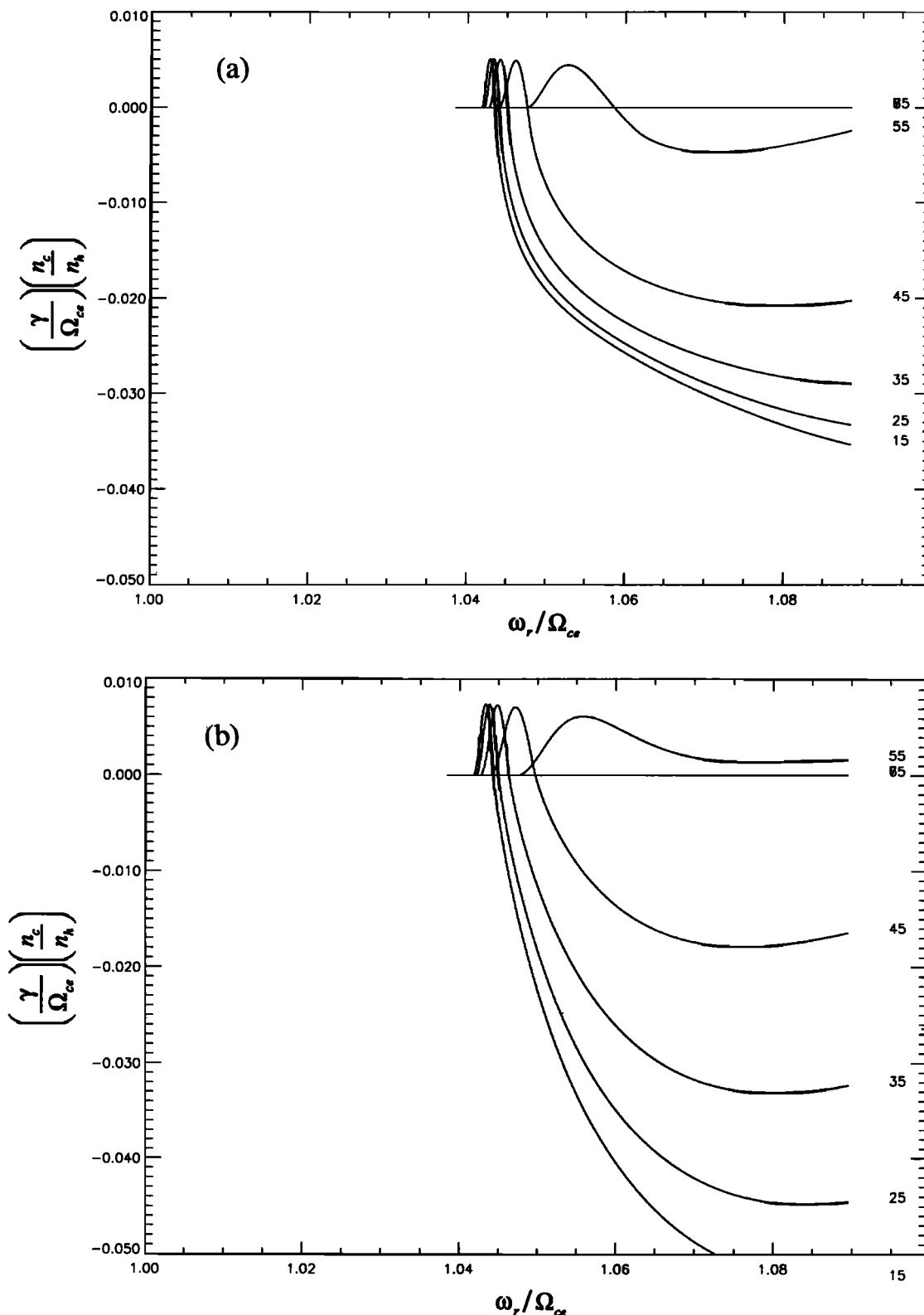
Figure 6. Same as Figure 5b except that $\Delta R_M/R_M$ is increased from 0.025 (an empty loss cone) to 0.63 (partially filled-in loss cone), with (a) $e\Delta\Phi/m_0c^2 = 0.0$ and (b) $e\Delta\Phi/m_0c^2 = 0.01$; slightly larger growth rates are obtained when there exists a large potential drop.

also evacuated. Although the CMI may be strengthened by the sharp loss cone boundary, the particle phase space density within the loss cone actually decreases as the loss cone is widened by a parallel potential drop. Furthermore, $\bar{\mu}$

is also increased slightly by the potential drop. Thus, contrary to the filled loss cone case discussed above, widening of an evacuated loss cone causes no enhancement of the CMI growth rate. For a constant n_h there are effectively
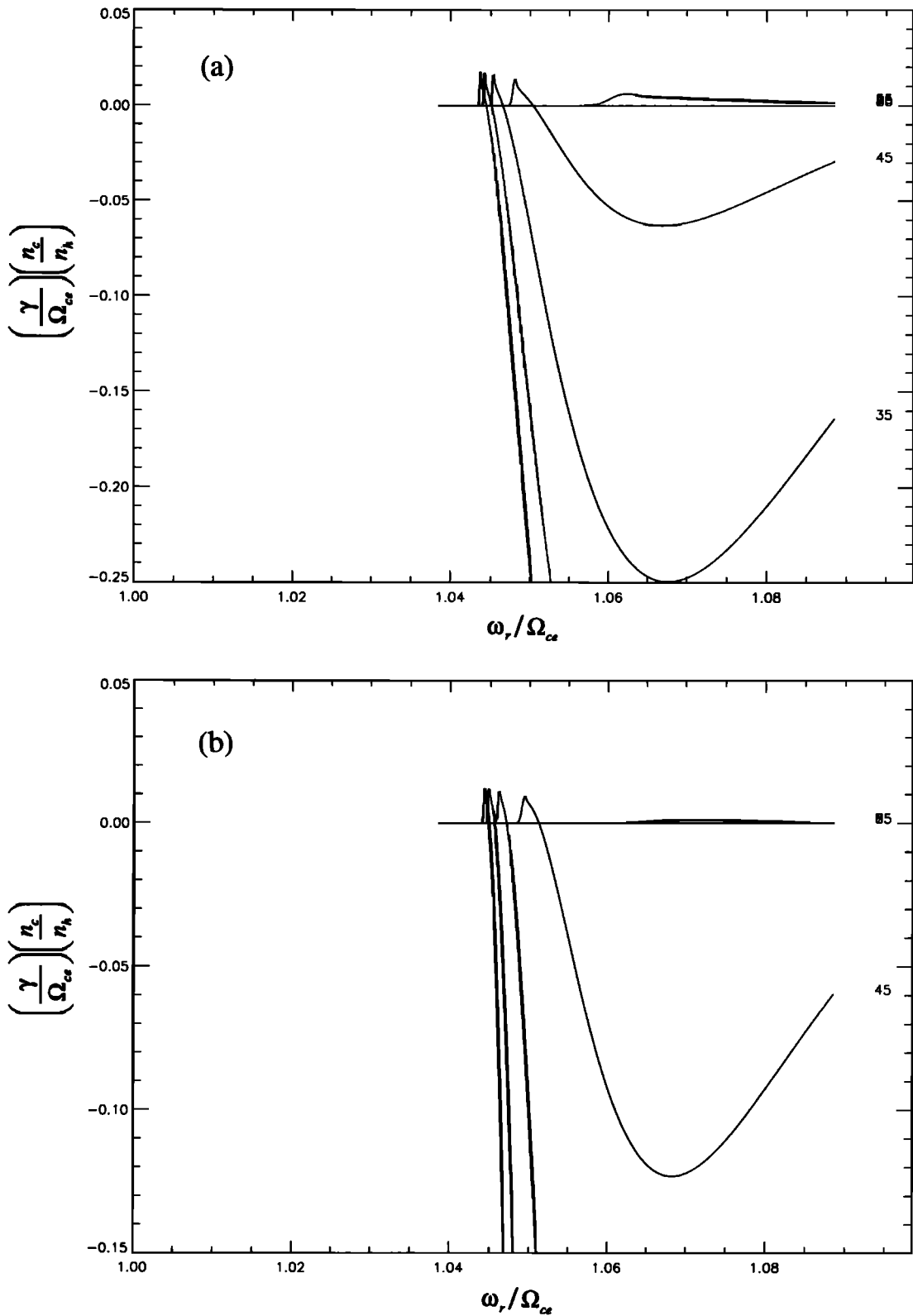
Figure 7. When ΔR_M is small (empty loss cone) the presence of a field-aligned potential drop, (a) $e\Delta\Phi/m_0c^2 = 0.002$ and (b) $e\Delta\Phi/m_0c^2 = 0.01$, below the observation point tends to enhance only the damping by the energetic electrons.

more particles outside the loss cone, causing an apparent increase of the damping by the energetic particles [*Omidi and Gurnett*, 1982, 1984].

We now turn our attention to the case when the energetic electrons possess a finite drift relative to the background

plasma, $u_0 \neq 0$ (Figure 4), such as in the accelerated plasma sheet particles ,*Gurgiolo and Burch*, 1988]. For $u_0 = 4\alpha$, $T_h = 1$ keV, and $\Delta R_M/R_M = 0.05$, Figures 8a for $e\Delta\Phi/m_0c^2 = 0.0$ and 8b for $e\Delta\Phi/m_0c^2 = 0.01$ show that large growth rates similar to Figure 5b can be obtained despite the smaller
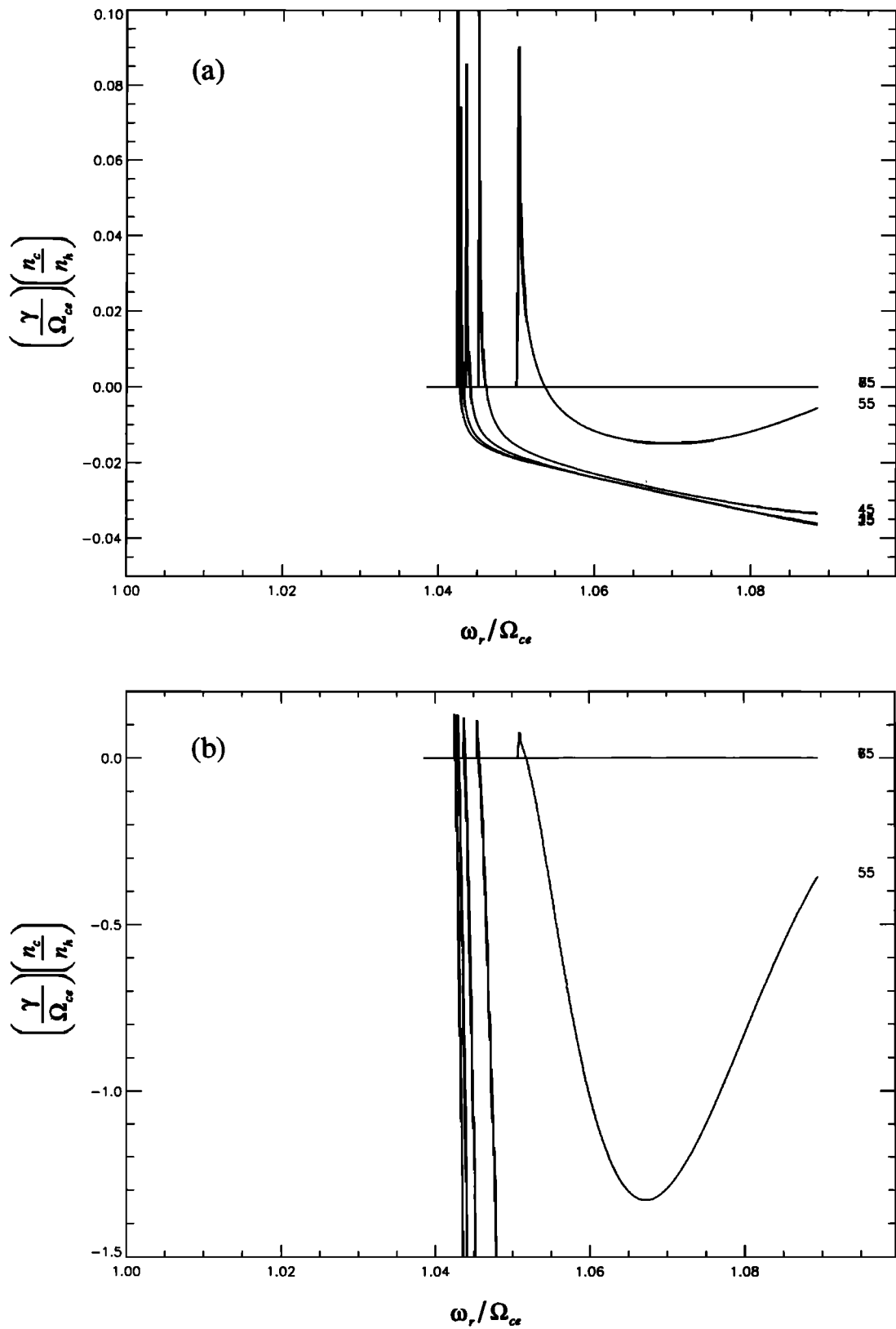
Figure 8. A finite momentum drift of $u_0 = 4\alpha$ in the electron distribution is sufficent for attaining large growth rates, despite the small ΔR_M and the presence of a field-aligned potential drop, (a) $e\Delta\Phi/m_0 c^2 = 0.0$ and (b) $e\Delta\Phi/m_0 c^2 = 0.01$.
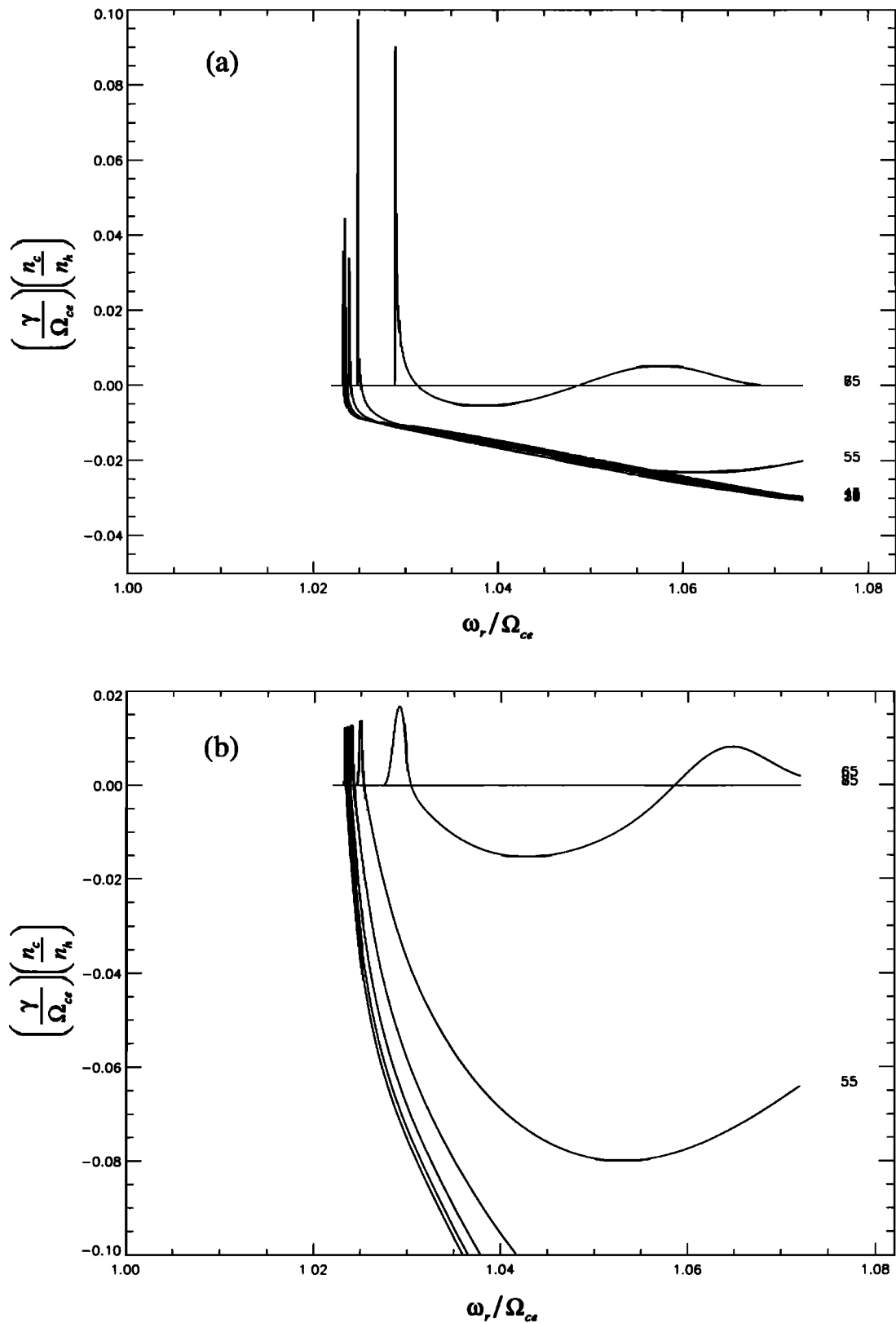
Figure 9. In addition to the usual filled-cone pattern with slightly lower frequencies at smaller wave normal angles (see Figure 5–8), multiple frequency peaks may be excited at the same wave normal angle; (a) and (b) different parameter sets (see Table 1).

loss cone (R has been increased from $1.5R_E$ to $2R_E$) and lower T_h. Again, there are no dramatic enhancements in the CMI growth rates as a result of the finite potential drop.

Finally, we investigate the emission and frequency patterns of the unstable waves as it is important for the interpretation of radio emission observations. In Figures 5–8 the emission pattern is a filled emission cone centered around the background magnetic field, with slightly lower frequencies emanating at smaller wave normal angles. Similar results have been obtained by *Wong et al.* [1982] and *Wu et al.* [1982] for the case of $n_h/n_c < 1$. However, they have also shown that when the energetic electrons dominate the plasma content, the excited waves will predominantly be in the oblique to normal directions.

We should note here that in the case of $n_h/n_c < 1$, the outward propagating waves may suffer absorption as they encounter weaker local magnetic fields, which may then result in a net hollow-cone emission pattern in the absence of wave scattering. This can be realized by considering the relativistic wave-particle resonance condition written as (see equation (7))

$$1 - \frac{m\Omega_e}{\gamma_L \omega_r} = n_z \frac{v_z}{c} \qquad (14)$$

For example, a field-aligned propagating wave ($n_z = n \approx 1$) will be damped by the background (with the strongest contribution coming from the $m = 1$ cyclotron harmonic), if it satisfies the relation that

$$1 - \frac{\Omega_e}{\gamma_L \omega_r} \approx \frac{v_z}{c} \qquad (15)$$

Since the wave encounters regions of decreasing Ω_e/ω_r as it traverses upward and away from the source, any wave damping by a cold background plasma will likely occur only near the source region where ω_r is closest to the local electron cyclotron frequency. For $T_e \leq 1$ eV we have $\gamma_L = 1$ and $v_z/c \leq 10^{-3}$. However, our growth rate calculations indicate that the unstable wave frequencies are such that $0.93 < \Omega_e/\omega_r < 0.98$, yielding $(1 - \Omega_e/\omega_r) \approx 10^{-2}$. Therefore damping of field-aligned propagating waves can be neglected for a sufficiently cold plasma.

On the other hand, Figures 9a and 9b show that multiple frequency peaks can also be excited at the same (oblique) wave normal angle (see the growth rate curves at 65° wave normal angle). The frequency separation of the two frequency components is of the order of a few percent of Ω_c at the source. We note further that the multiple peak feature is present even when $u_0 = 0$. Similar double frequency peaks have also been obtained by *Omidi and Gurnett* [1982, 1984] from loss cone distributions observed in the Earth's auroral zone. Thus an emission characteristics of the loss cone distribution is that the fundamental X mode waves can be excited simultaneously within the field-aligned emission cone and in the oblique directions at slightly higher frequencies.

Let us now discuss briefly the generation of AKR in terms of our growth rate calculations. We pointed out earlier that our calculations assumed small density ratios, $n_h/n_c < 1$. However, it is generally known that the parallel electric fields inside auroral density cavities will deplete the low-energy background plasma such that the energetic electrons usually form the major electron component within the au-

roral acceleration region, where strong AKR sources have been observed [*Ungstrup et al.*, 1990; *Hilgers et al.*, 1992]. Therefore the results of our calculations are strictly inapplicable to explaining the generation of AKR from the interior of the auroral density cavities.

The small density ratio approximation may be applicable near the edges of the auroral density cavities. From observations by the Viking satellite at altitudes of 6500–8500 km (i.e., $R \approx 2R_E$ as in the parameters used for our calculations, see Table 1), *Hilgers et al.* [1992] determined that n_c and n_h near the centers of auroral density cavities are comparable and are usually limited to <0.35 cm^{-3}. Outside the cavities, n_c increases to 15 cm^{-3} ($\omega_{pc}/\Omega_c = 0.2$, see Table 1) or higher with n_h dropping precipitously. These observations indicate that the energetic-to-background electron density ratios near the edges of auroral density cavities may well have been $n_h/n_c \leq 10^{-2}$, adequate for providing sufficiently high growth rates to explain the generation of AKR (see discussion above).

Conclusions

We have investigated the electron cyclotron maser instability (CMI) driven by a drift-loss cone distribution (equation (1)) such as that exhibited by the accelerated plasma sheet electrons (Figure 2) [*Gurgiolo and Burch*, 1988]. From this study we conclude that

1. The DGH distibution (Figure 1) does not give a proper representation of an observed loss cone distribution and may, however, be more appropriate for modeling the trapped population on auroral field lines. Moreover, it cannot be readily used to study the effects of a parallel potential drop on the loss cone boundary.

2. For a true loss cone (equations (1a) and (1b)) the width of the loss cone boundary can be modeled in terms of the "fuzziness" of the mirror point location at low altitudes (equation (3)), larger widths weaken the CMI (Figures 5b and 6a).

3. The presence of a parallel potential drop increases only slightly the CMI growth rates excited by a partially filled loss cone (large $\Delta R_M/R_M$) (Figure 6), and it enhances the damping due to the energetic electrons for an evacuated loss cone (small $\Delta R_M/R_M$) (Figure 7).

4. A finite u_0 or relatively hot energetic electrons are needed to attain sufficiently large growth rates ($\gamma/\Omega_{ce} \sim 10^{-3}$) (Figure 8).

In the limit that the energetic electrons are tenuous ($10^{-3} < n_h/nc < 1$) our linear growth rates calculations indicate that the fundamental X mode excited by the CMI are characterized by the following:

5. A filled emission cone (up to $\sim 120°$ wide) formed by the waves with frequencies near the R-X cutoff, with lower-frequency waves being more field-aligned (Figure 5–8). Similar results have been obtained by *Wong et al.* [1982] and *Wu et al.* [1982] in the low density ratio limit.

6. Higher-frequency waves can be excited from the same source region (loss cone) at the same wave normal angle as the lower-frequency components, possibly with a reversed angular distribution with frequency (Figure 9); may be applicable to the fine structure AKR [*Gurnett and Anderson*, 1979; *Benson et al.*, 1988].

7. These emission characteristics may be relevant to waves generated at edges of the auroral density cavities. The

resulting wave intensities may be comparable to those generated near the centers of the density depletion.

References

Benson, R. F., M. M. Mellot, R. L. Huff, and D. A. Gurnett, Ordinary mode auroral kilometric radiation fine structure observed by DE 1, *J. Geophys. Res.*, *93*, 7515, 1988.

Croley, D. R., P. F. Mizera, and J. F. Fennell, Signature of a parallel electric field in ion and electron distributions in velocity space, *J. Geophys. Res.*, *83*, 2701, 1978.

Dory, R. A., G. E. Guest, and E. G. Harris, Unstable electrostatic waves propagating perpendicular to a magnetic field, *Phys. Rev. Lett.*, *14*, 131, 1965.

Gaelzer, R., L. F. Ziebell, and R. S. Schneider, Propagation and amplification of auroral kilometric radiation in finite width auroral cavity, *J. Geophys. Res.*, *97*, 19,299, 1992.

Gurgiolo, C., and J. L. Burch, Simulation of electron distribution within auroral acceleration regions, *J. Geophys. Res.*, *93*, 3989, 1988.

Gurnett, D. A., and R. R. Anderson, The kilometric radio emission spectrum: Relationship to auroral acceleration processes, in *Physics of Auroral Arc Formation, Geophys. Monogr. Ser.*, vol. 25, edited by S.-I. Akasofu and J. R. Kan, p. 341, AGU, Washington, D. C., 1979.

Hewitt, R. G., D. B. Melrose, and K. G. Rönnmark, The loss-cone driven electron-cyclotron maser, *Aust. J. Phys.*, *35*, 447, 1982.

Hilgers, A., B. Holback, G. Holmgren, and R. Boström, Probe measurements of low plasma densities with applications to the auroral acceleration region and auroral kilometric radiation sources, *J. Geophys. Res.*, *97*, 8631, 1992.

Krall, N. A., and A. W. Trievelpiece, *Principles of Plasma Physics*, p. 389, McGraw-Hill, New York, 1973.

Le Quéau, D., and P. Louarn, Analytic study of the relativistic dispersion: application to the generation of the auroral kilometric radiation, *J. Geophys. Res.*, *94*, 2605, 1989.

Louarn, P., A. Roux, H. de Féraudy, D. Le Quéau, M. André, and L. Matson, Trapped electrons as a free energy source for the auroral kilometric radiation, *J. Geophys. Res.*, *95*, 5983, 1990.

Menietti, J. D., J. L. Burch, R. M. Winglee, and D. A. Gurnett, DE 1 particle and wave observations in auroral kilometric radiation (AKR) source regions, *J. Geophys. Res.*, *98*, 5865, 1993.

Montgomery, D. C., and D. A. Tidman, *Plasma Kinetic Theory*, p. 137, McGraw-Hill, New York, 1964.

Mourenas, D., V. V. Krasnosel'skikh, and C. Beghin, Semirelativistic maser cyclotron instabilities in multicomponent plasmas, *J. Geophys. Res.*, *98*, 5855, 1993.

Omidi, N., and D. A. Gurnett, Growth rate calculations of auroral

kilometric radiation using the relativistic resonance condition, *J. Geophys. Res.*, *87*, 2377, 1982.

Omidi, N., and D. A. Gurnett, Path-integrated growth of auroral kilometric radiation, *J. Geophys. Res.*, *89*, 10,801, 1984.

Persoon, A. M., D. A. Gurnett, W. K. Peterson, J. H. Waite, Jr., J. L. Burch, and J. L. Green, Electron density depletions in the nightside auroral zone, *J. Geophys. Res.*, *93*, 1871, 1988.

Persson, H., Electric field parallel to the magnetic field in a low density plasma, *Phys. Fluids*, *9*, 1090, 1966.

Reiff, P. H., H. L. Collins, J. D. Craven, J. L. Burch, J. D. Winningham, E. G. Shelly, L. A. Frank, and M. A. Friedman, Determination of auroral electrostatic potentials using high- and low-particle distributions, *J. Geophys. Res.*, *93*, 7441, 1988.

Sharma, R. R., L. Vlahos, and K. Papadopoulos, the importance of plasma effects on electron-cyclotron maser-emission from flaring loops, *Astron. Astrophys.*, *112*, 377, 1982.

Stix, T. H., *Waves in Plasmas*, p. 5, American Institute of Physics, New York, 1992.

Tsai, S. T., C. S. Wu, Y. D. Wang, and S. W. Kang, Dielectric tensor of a weakly relativistic, nonequilibrium, and magnetized plasma, *Phys. Fluids*, *24*, 2186, 1981.

Ungstrup, A., Bahnsen, H. K. Wong, M. Andre, and L. Matson, Energy source and generation mechanism for auroral kilometric radiation, *J. Geophys. Res.*, *95*, 5973, 1990.

Winglee, R. M., and P. L. Pritchett, The generation of low-frequency electrostatic waves in association with auroral kilometric radiation, *J. Geophys. Res.*, *91*, 13,531, 1986.

Wong, H. K., C. S. Wu, F. J. Ke, R. S. Schneider, and L. F. Ziebell, Electromagnetic cyclotron-loss-cone instability associated with weakly relativistic electrons, *J. Plasma Phys.*, *28*, 503, 1982.

Wong, H. K., D. Krauss-Varban, and C. S. Wu, On the role of the energy of suprathermal electrons in the generation of auroral kilometric radiation, *J. Geophys. Res.*, *94*, 5327, 1989.

Wu, C. S., Kinetic cyclotron and synchrotron maser instabilities: Radio emission processes by direct amplification of radiation, *Space Sci. Rev.*, *41*, 215, 1985.

Wu, C. S., and L. C. Lee, A theory of the terrestrial kilometric radiation, *Astrophys. J.*, *230*, 621, 1979.

Wu, C. S., and X. M. Qiu, Emission of second-harmonic auroral kilometric radiation, *J. Geophys. Res.*, *88*, 10,072, 1983.

Wu, C. S., H. K. Wong, D. J. Gorney, and L. C. Lee, Generation of the auroral kilometric radiation, *J. Geophys. Res.*, *87*, 4476, 1982.

Yoon, P. H., and D. Krauss-Varban, Gyroharmonic maser instability for weakly relativistic electrons with a loss-cone distribution, *Phys. Fluids B*, *2*, 1918, 1990.

S. F. Fung, Space Physics Data Facility, NASA Goddard Space Flight Center, Greenbelt, MD 20771. (e-mail: Internet fung@nssdca.gsfc.nasa.gov)

A. F. Viñas, Laboratory of Extraterrestrial Physics, NASA Goddard Space Flight Center, Greenbelt, MD 20771. (e-mail: Internet uzafv@lepafv.gsfc.msa.gov)